Materials Science and Engineering: A
Volume 763, 19 August 2019, 138072

Atomic structure and interface chemistry in a high-stiffness and high-strength Al–Si–Mg/TiB_2 nanocomposite

ShouxunJi[a] Fateme Amirkhanlu[b] Ali Mostaed[cd] Richard Beanland[d]
a Brunel Centre for Advanced Solidification Technology (BCAST), Brunel University London, Uxbridge, Middlesex, UB8 3PH, UK
b Department of Mining and Metallurgical Engineering, Amirkabir University of Technology, Tehran, Iran
c Department of Materials Science and Engineering, University of Sheffield, Sheffield, S1 3JD, UK
d Department of Physics, University of Warwick, Gibbet Hill Road, CV4 7AL, Coventry, UK

Abstract

We investigate a new generation of aluminium alloys, Al–Si–Mg/TiB_2 nanocomposites, with both high stiffness (Young's modulus 94 GPa) and high yield strength (322 MPa), designed for automotive applications. A significant weight reduction (>30%) can be achieved by these nanocomposites compared with conventional Al alloys in components designed for stiffness. The crystallography and distribution of TiB_2 particles and β″ precipitates, as well as the chemistry and structure of Al/TiB_2 interfaces, have been characterized at atomic scales. The TiB_2 nanoparticles (average particle size ~450 nm), the main cause of stiffness improvement, were homogeneously distributed within the Al–Si–Mg matrix. The interfaces between Al and TiB_2 nanoparticles were mainly parallel to dense planes of the TiB_2, including basal {0001}, prismatic $\{11\bar{0}0\}$ and pyramidal $\{01\bar{1}1\}$ planes. All facets show a transitional zone in the alloy matrix, roughly 1 nm in thickness. We also find a Cu-rich layer (~2 at.%) on pyramidal $\{01\bar{1}1\}$ facets. The β″ precipitates are the main cause of high yield strength and work in conjunction with TiB_2 nanoparticles to produce an alloy with outstanding mechanical properties.

Keywords

Nanocomposite
Aluminium alloys
Interface structure

Mechanical properties

Stiffness

Atomic resolution STEM

1. Introduction

The automotive industry is currently seeking significant weight reduction for structural aluminium-based components in which Young's modulus (E) and yield strength (YS) are the main design criteria [1,2]. These alloys, generally used in cast form, must have high yield strength and materials improvement in past decades has focused almost exclusively on improvement of this parameter. Nevertheless, a high Young's modulus allows a reduced wall thickness and hence the volume of material in components [3]. Young's modulus is often simply taken as an intrinsic property that can only be affected marginally by alloying additions. For example, Be [4], Li [5], Si [6], Cu [7] and Ni [8] are known to raise the stiffness of Al alloys slightly, while Mg [9] decreases it. Overall, the increase of Young's modulus through adding alloying elements is usually less than 10% in Al alloys, while the presence of strengthening defects such as dislocations and internal interfaces usually lowers the stiffness [10]. Thus, the low Young's modulus value of commercial Al alloys (~70 GPa) often needs to be compensated by a larger wall thickness and the potential weight reduction provided by these light alloys is not realised. Future materials improvement must consider both E and YS of structural components in order to reduce CO_2 emission and fuel consumption [11]. In recent years, several research groups have started to develop high modulus and high strength Al–TiB_2 composites through in-situ formation of high modulus phases in the microstructure [12,13]. Different aspects of these composites, such as solidification [2], interface structure [14] and deformation [15] has been investigated. TiB_2 is one of the most popular reinforcements for high modulus AMCs because of its Young's modulus of 560 GPa and its easy synthesis using an in-situ process. Kumar et al. [16] reported an increase of 108% in hardness, 123% in yield strength and 43% in UTS of the Al–7Si cast alloy with 10 wt% of TiB_2. Han et al. [17] studied the tensile properties of the Al–12Si alloy with 4 wt% TiB_2 particles and found that the improvement of the strength can be observed in the temperature range of 25–350 °C.

A promising pathway to overcome design limits, and in particularly to raise the Young's modulus, lies in creating nanocomposite microstructures, i.e. formation of stiff nanoparticles in the Al matrix. This is due to the fact that only a high modulus nano phase can significantly improve both YS and E in Al alloys. In fact, Young's modulus and yield strength of Al alloys

can only be improved when four key factors are fully satisfied: (1) a large volume fraction of the high modulus phases; (2) strong interfacial bonding between Al and the high modulus phases; and (3) homogeneous distribution of the reinforcement [18,19]. Based on these factors, a new generation of aluminium alloys can be developed for automotive applications. Thus far, the main purpose of Al alloys with added high modulus particles such as SiC and Al_2O_3 has been improvement of wear resistance and/or high temperature performance [20]. It is very important to carefully and specifically select the type, size as well as volume fraction of reinforcements for E and YS improvement. In this work, titanium diboride (TiB_2) has been selected as a reinforcement material due to three important reasons. First, it has the highest Young's modulus (E = 565 GPa [21]) among the available ceramic phases for casting; and only 9 vol% of TiB_2 can potentially lead to at least 30% increase in the specific stiffness E/ρ of Al alloys [22]. Second, TiB_2 nanoparticles can significantly increase the Orowan strengthening mechanism. Finally, it is possible to form TiB_2 nanoparticles in bulk components through in-situ reactions during a commercial casting process.

The primary use of TiB_2 in Al alloys has been as a grain refiner, and dates back some time [23,24]. Al/TiB_2 composites, synthesised through an in-situ reaction between K_2TiF_6 and KBF_4 salts in molten Al, have been in use since the 1990s [25]. These reactions have been reported as follows [25]:

(1)3K2TiF6+13Al→3TiAl3+3KAlF4+K3AlF6(2)2KBF4+3Al→AlB2+2KAlF4(3)AlB2+TiAl3→TiB2+4Al

The Gibbs free energy for formation of TiB_2 is lower than that of other phases such as Al_3Ti and AlB_2 [26], which provides a thermodynamic driving force for the formation of TiB_2 over an appropriate reaction time (20–30 min) and temperature (~850 °C) prior to solidification. The *P*6/*mmm* TiB_2 precipitates crystallise in the Al melt prior to solidification in the form of hexagonal platelets or prisms. Various Al alloys reinforced by TiB_2 particles have been synthesised, however, all of the existing studies are concentrated on grain refinement [27], subsequent processing methods [28], thermodynamic evaluations [[29], [30], [31], [32], [33]], strength improvement [34], wear performance [35] and high-temperature properties [36]. In-situ TiB_2 particles in Al alloys synthesised to date are typically 0.2–4 μm in size [37,38] and their volume fraction is usually less than 4 vol%, which does not produce any significant improvement of stiffness [[39], [40], [41], [42], [43], [44]]. Improvement of YS by formation of in-situ TiB_2 particles in cast Al alloys has been well documented [36,45], although these alloys rarely exceeded 300 MPa yield strength. For example, Han et al. [36] reported

240 MPa yield strength (an increase of 10%) in the Al–12Si–4Cu–3Ni-0.8 Mg cast alloy, with 4 vol% of TiB_2.

The aim of this work is to understand the crystallography of the formed nanoparticles, the interface chemistry and structure at the principal facets of matrix/reinforcement and the strengthening mechanisms. These are essential steps required to produce a novel high modulus and high strength Al-based alloy. The crystallography and distribution of TiB_2 particles, as well as the chemistry and atomic structure of interfaces between TiB_2 particles and the Al matrix, are analysed using state of the art atomic resolution characterization techniques and benchmarked against the aforementioned four key factors. The Young's modulus and yield strength of the observed microstructure are analysed using micromechanics-based models, and calculations are compared with the experimental data. The contribution of different strengthening mechanisms to the YS of the experimental materials is also discussed.

2. Materials and methods

2.1. Nanocomposite preparation

Aluminium ingots were melted in a clay-graphite crucible using an electric resistance furnace. An Al–Si–Mg alloy was produced by adding Si in the form of Al–50Si master alloy and pure magnesium to form either Al–7Si-0.3 Mg or Al–10Si-0.3 Mg (all compositions are in wt.% unless otherwise specified). A mixture of KBF_4 and K_2TiF_6 salts was then added in accordance with 1Ti:2B atomic ratio to produce Al–7Si-0.3Mg/8 vol% TiB_2, Al–7Si-0.3Mg/9 vol% TiB_2 and Al–10Si-0.3Mg/9 vol% TiB_2 composites. Other minor alloying elements of the three composites were unchanged (0.1 Ti, <0.1 Fe, <0.1 Cu, <0.01 Ni, <0.05 Mn and <0.05 Zn). The melt's temperature was maintained at 850 °C for 30 min to complete the exothermic TiB_2 solidification [46]. After 1 h of homogenisation at 740 °C, the molten metal was then degassed using pure argon injected into the melt by means of a rotary degassing impeller at a speed of 350 rpm for 4 min. After degassing, the top surface of the melt was covered by commercial granular flux, and then the melt was held for 15 min for temperature recovery. The melt was then poured into a preheated permanent mould designed according to the ASTM B-108 standard [47]. The casting method was a low pressure die casting (LPDC) [48]. The alloys were then solution-treated at 545 °C for 9 h, quenched in cold water and aged at 180 °C for 9 h to achieve T6 condition. Multiple preparation runs were performed to check the reproducibility of the resulting materials. The Al–7Si-0.3 Mg alloy

was chosen as a reference material for comparison because it has been broadly used in industry and can be considered as a representative conventional cast Al alloy.

2.2. Characterization

X-ray diffraction (XRD) patterns were recorded by a D8 advance Bruker X-ray diffractometer (Bruker Corporation, Billerica, Massachusetts, United States) with CuK_{α} radiation in the range of 2 theta = 20–90° using a step size of 0.05° and a time of 1s per step. XRD patterns were analysed using X'Pert High Score software (X'Pert V2.2, PANalytical, Almelo, The Netherlands). Microstructural analysis was performed by high-resolution field emission transmission electron microscope (HR-FETEM, JEOL 2100F, JEOL Ltd. Tokyo, Japan) as well as an aberration-corrected scanning transmission electron microscope (STEM, JEOL ARM200F, JEOL Ltd. Tokyo, Japan) operating at 200 kV. On the latter microscope atomic resolution energy dispersive X-ray (EDX) spectroscopy measurements were obtained with a windowless Oxford Instruments X-max 100 SDD x-ray detector. TEM specimens were prepared using standard routes, i.e. mechanical grinding and polishing followed by ion milling using a Gatan precision ion polishing system (PIPS) at 5.0 kV and at an incident angle of 4°. The DetectColumns program [49] was used to calculate the atom columns' intensities in the atomic resolution STEM images obtained from our samples. To observe the morphology of TiB_2 particles by field-emission scanning electron microscopy (SEM, SUPRA 35VP, Carl-Zeiss Company, Oberkochen, Germany), the specimens were deep etched by 20 vol% NaOH solution for 5 min. Clemex Vision Image analysis software (Clemex V2.0, Clemex Technologies Inc. Longueuil, Canada) was utilized to determine different attributes of the reinforcement, precipitates and grains on images acquired by SEM, TEM and optical microscopy. These included the volume fraction of reinforcement and precipitates, average α-Al grain and precipitate/particle sizes, and the aspect ratio of reinforcement particles. The average size of particles and grains was defined as the diameter of a circle having the same area as that of the particle and was calculated using Eq. (4). The aspect ratio of particles was measured as the ratio of the length of its longest feret to the length of its shortest feret. The average diameter and aspect ratio were taken from at least 200 measurements.(4)Averagediameter=4(Area)π

The Young's modulus of the specimens was measured by the ultrasonic pulse technique according to ASTM E1875-13 [50]. Parallel smooth surfaces in the specimens were shaped by grinding and polishing before measuring the transversal and longitudinal wave velocities. The wave velocities of the specimens were measured using a 38DL PLUS Ultrasonic

Thickness Gage (Olympus Industrial) and the Poisson's coefficient (ϑ) and Young's modulus (E) were calculated according to the following equations [51]:

Poisson's ratio(5)

(ϑ)=1−2(VT/VL)22−2(VT/VL)2(6)Young′smodulus(E,GPa)=VL2ρ(1+ϑ)(1−2ϑ)1−ϑwhere V T is transverse velocity, VL is longitudinal velocity and ρ is density. Tensile tests were conducted according to ASTM E8/E8M [52] using an Instron 5500 Universal Electromechanical Testing Systems equipped with Bluehill software and a ±50 kN load cell. All tensile tests were performed at room temperature. The gauge length of the extensometer was 50 mm and the ramp rate for extension was 1 mm/min.

3. Results

3.1. Analysis of nanoparticles

TEM micrographs of the Al–Si–Mg/TiB_2 composites (Fig. 1) show the reinforcing nanoparticles are homogeneously distributed in the Al alloy matrix. The size of particles is in the range of 20–3000 nm and their average size is about 480, 450 and 420 nm for Al–7Si-0.3Mg/8 vol% TiB_2, Al–7Si-0.3Mg/9 vol% TiB_2 and Al–10Si-0.3Mg/9 vol% TiB_2, respectively. In addition, the measured volume fraction of the particles in the SEM images of the composites using Clemex image analysis software is 7.8%, 8.9% and 8.8% for Al–7Si-0.3Mg/8 vol% TiB_2, Al–7Si-0.3/9 vol% TiB_2 and Al–10Si-0.3Mg/9 vol% TiB_2 nanocomposites, respectively, which is in good agreement with the nominal chemical composition. Three different phases can be seen in the X-ray diffraction patterns of Fig. 2, i.e. α-Al, Si and TiB_2, while the reference Al–7Si-0.3 Mg alloy with no nanoparticle additions has only α-Al and β-Si. The characteristic peaks of the Al–Si–Mg/TiB_2 nanocomposites have high intensities and are well matched with JCPDS cards (α-Al, No. 00-001-1180, β-Si, No. 01-080-0018 and TiB_2, No. 01-075-0967).

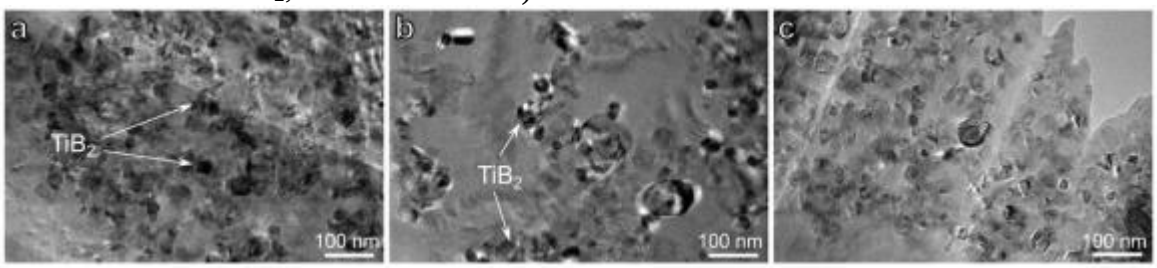

Fig. 1. Typical TEM images of (a) Al–7Si-0.3Mg/8 vol% TiB_2, (b) Al–7Si-0.3Mg/9 vol% TiB_2 and (c) Al–10Si-0.3Mg/9 vol% TiB_2 nanocomposites, showing relatively homogeneous distribution of TiB_2 nanoparticles.

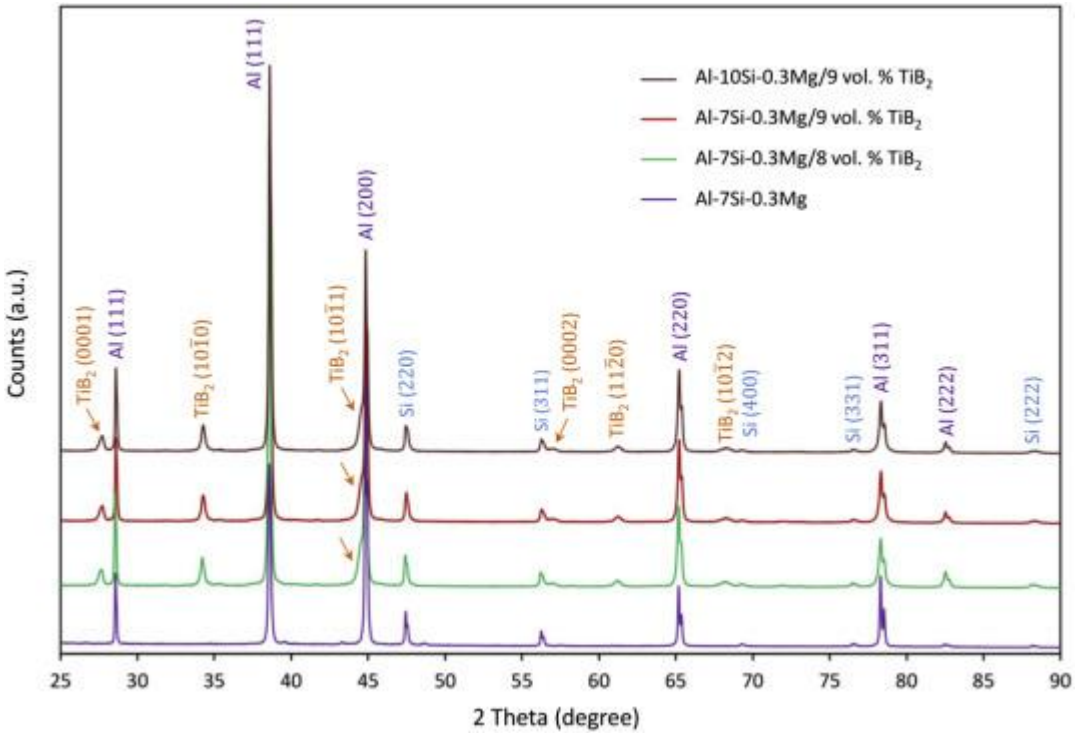

Fig. 2. X-ray diffraction patterns of the Al–Si–Mg alloy and its composites reinforced by TiB_2 nanoparticles with clear Al, Si and TiB_2 peaks.

Since TiB_2 and AlB_2 are isomorphic, with similar lattice parameters (ÅÅÅÅaTiB2=3.028Å,cTiB2=3.288Å;aAlB2=3.003Å,cAlB2=3.254Å) and XRD data give us average lattice parameters for all the nanoparticles, a complementary crystallographic and chemical analysis of the nanoparticles was performed on several particles by EDX analysis (e.g. Fig. 3b) and selected area diffraction (SAD) combined with tilting [53] (e.g. Fig. 3c–f). A representative TEM bright field micrograph from Al–10Si-0.3Mg/9 vol% TiB_2 nanocomposite, together with EDX data and SAD patterns taken from the indicated particle at three different low-index zone axes are shown in Fig. 3. The EDX data confirm that the particles displayed in the TEM image are Ti rich particles. In addition, all the SAD patterns, taken from the particle marked in Fig. 3a, were indexed as *P*6/*mmm* TiB_2 and the angles between the zone axes agree with the corresponding tilting angles as illustrated in the stereographic Kikuchi map in Fig. 3f. The *d*-spacing values measured from SAD patterns are very close to the values provided in PDF standard card data, as listed in Table 1. The SAD and EDX results confirm that the reinforcing nanoparticles are the hexagonal TiB_2 phase.

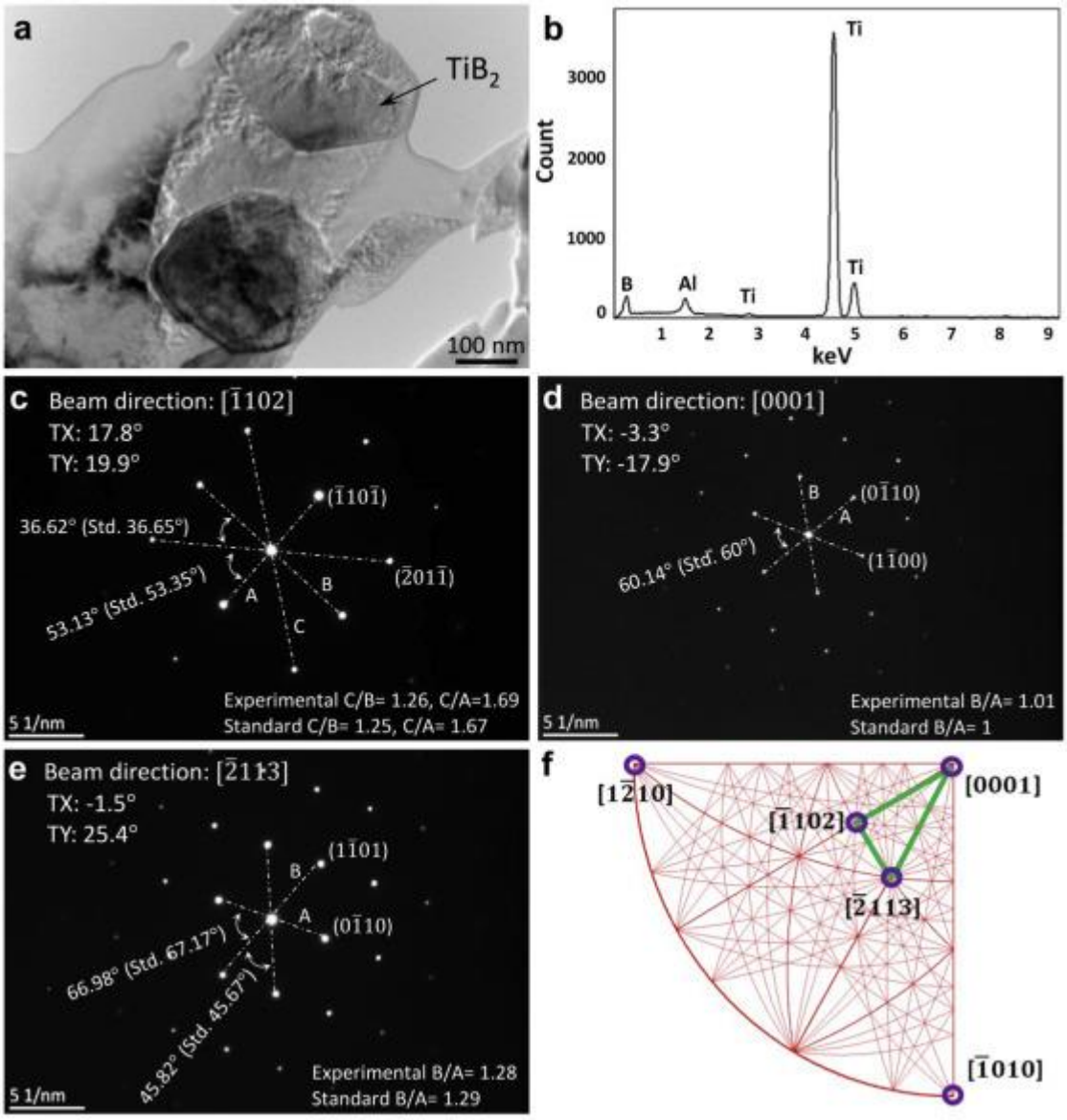

Fig. 3. (a) Typical TEM bright field micrograph of TiB_2 nanoparticles taken from Al–10Si-0.3Mg/9 vol% TiB_2 nanocomposite. (b) EDX profile as well as its corresponding quantitative results acquired from the particle pointed by an arrow shown in (a). SADPs obtained from the particle denoted as TiB_2 in (a) along different beam directions (BDs): (c) [1^{-}102], (d) [0001] and (e) [2^{-}113]. (f) The corresponding stereographic Kikuchi line map.

Table 1. Comparison of the interplanar spacing (*d*-spacing) and 2theeta values between SADP standard for TiB_2.

Plane	*d*-spacing (nm), SADP	d-spacing (nm), PDF	2Theeta (degree)	2Theeta (degree), PDF
($11^{-}00$)	0.2611 ± 0.0026	0.2622 ± 0.0013	34.153	34.165
($11^{-}01$)	0.2021 ± 0.0020	0.2035 ± 0.0010	44.431	44.447

Fig. 4a displays an SEM image of a deep etched sample, where the Al matrix has been etched leaving TiB_2 particles on the surface that can be seen easily. As shown, the TiB_2 particle has a hexagonal morphology. A high-resolution STEM image in Fig. 4b shows a TiB_2 particle embedded in the Al matrix with hexagonal shape and a chamfered edge. The TiB_2 particles are facetted with basal {0001}, prismatic {$11\bar{0}0$} and pyramidal {$011\bar{1}$} facets, as shown schematically in Fig. 4c. This is consistent with previous observations [54] and theoretical growth morphologies [55].

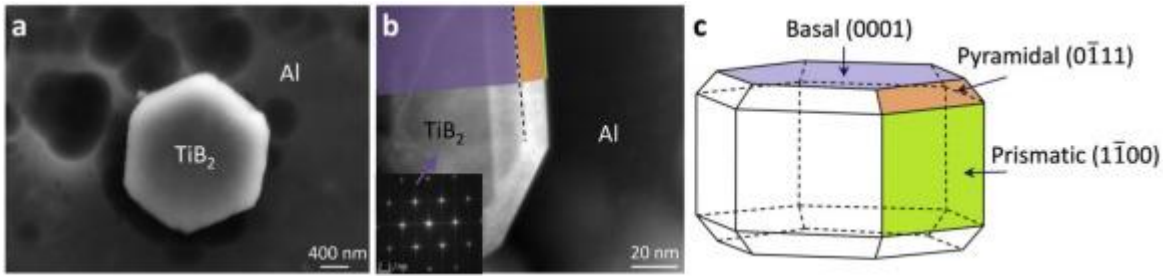

Fig. 4. (a) SEM micrograph showing the hexagonal morphology of the TiB_2 particles in a deep etched Al–Si–Mg/TiB_2 nanocomposite, (b) STEM image showing the morphology of a TiB_2 particle viewed along {0001} with chamfered edge and its typical basal {0001}, prismatic {$11\bar{0}0$} and pyramidal {$011\bar{1}$} facets, and (c) schematic morphology and facets of TiB_2 particles.

3.2. Interface structure and chemistry

Fig. 5 shows ADF- and BF-STEM images obtained from a basal {0001} interface between a TiB_2 nanoparticle and Al alloy. In this figure, the TiB_2 crystal is viewed along [$112\bar{0}$] while the Al alloy matrix is viewed ~5° away from [211], i.e. the interface is incoherent without a well-defined orientation relationship between the particle and matrix. Although the interface seems flat, a faint extension of the nanoparticle lattice can be seen several monolayers into the Al matrix. This is consistent with an interfacial roughness of ~1 nm, as shown by the yellow dashed line in Fig. 5d, or indeed the presence of a coherent $Al_xTi_{1-x}B_2$ interfacial layer. Periodic contrast variations are also visible along the interface, probably indicating the presence of a misfit dislocation array.

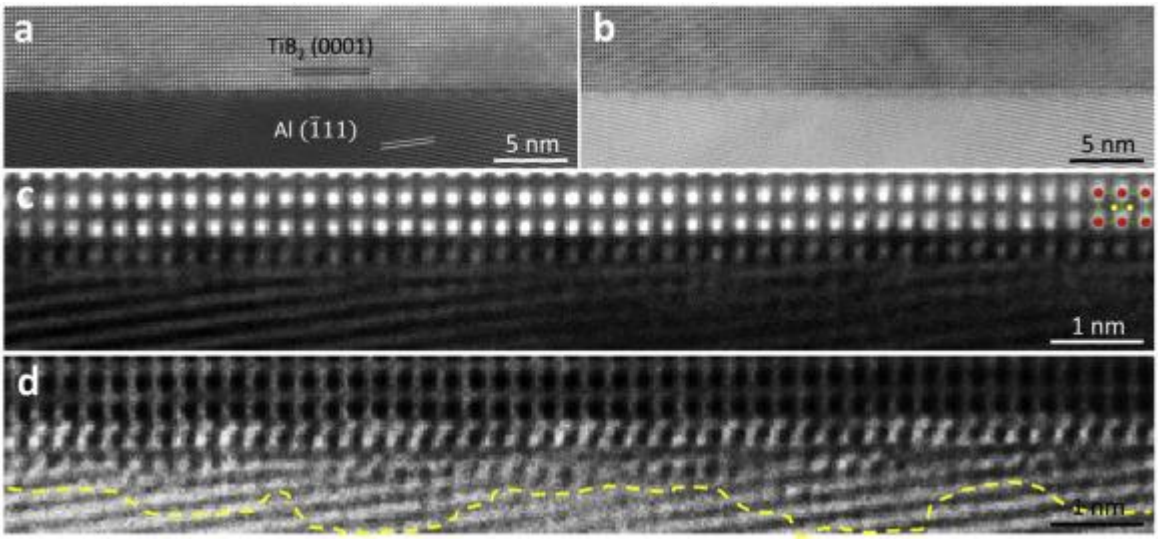

Fig. 5. High resolution ADF-STEM (a and c) and BF-STEM (b and d) images of Al/TiB_2 interface parallel to the basal plane (0001) of TiB_2 when the incident electron beam is parallel to [$11\bar{2}0$] for TiB_2 and ~5° to [211] for Al. A model of TiB_2 is superimposed on (c); Ti and B atoms are represented in red and yellow, respectively.

STEM images from another basal plane TiB_2 interface, in which TiB_2 is viewed along [$21\bar{3}0$], are shown in Fig. 6a and b. Here, the Al matrix is not viewed along any crystallographic axis and so no lattice can be seen. Yet again, a faint nanoparticle lattice appears to extend beyond the edge of the nanoparticle, which is obvious in the ADF image by the bright (relatively high Z) Ti atom columns. To show this more clearly, the mean Voronoi intensity of Ti atom columns from each (0001) plane in the ADF image (T0 to T10 in Fig. 6a) are plotted in Fig. 6c. The (0001) layers of Ti inside the TiB_2 particle (T4 to T10) are uniformly bright. The intensity drops from layer T3. Layer T2 has ~2% lower intensity, T1 ~6% lower intensity and T0 has only 60% of the intensity of layers inside the particle. Although it is clear that there is some overlap of Al matrix and this interface – the {110}Al planes continue up to the interface and indeed over the particle – the large decrease in the intensity of these atom columns suggests that a commensurate monolayer or two of Ti-rich material is present at the nanoparticle/matrix interface.

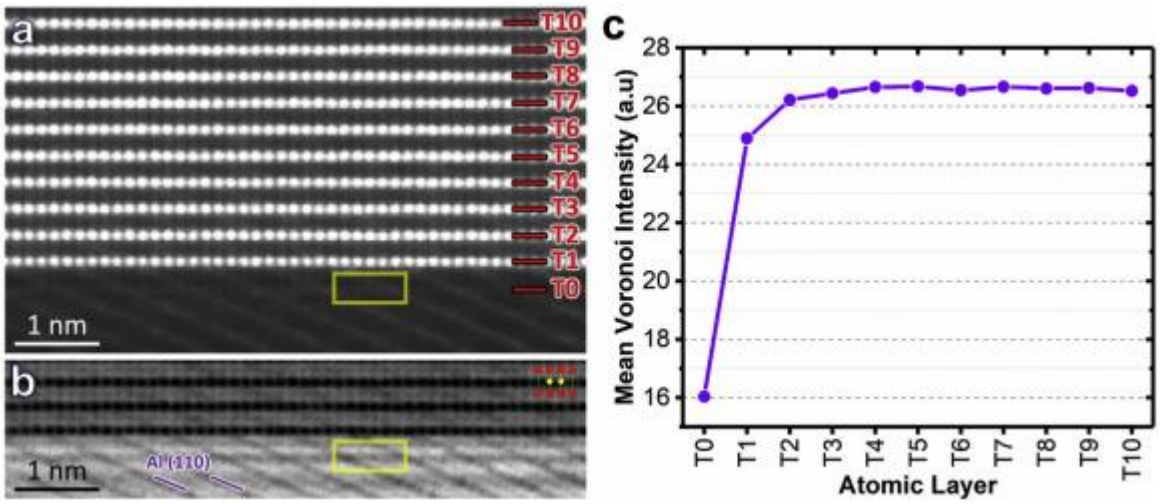

Fig. 6. High resolution (a) ADF-STEM and (b) BF-STEM images of an (0001) TiB_2/Al interface. The incident electron beam is parallel to [213¯0] for TiB_2 and ~9° from [001] for Al, where only (110) fringes can be seen. A model of TiB_2 is superimposed onto (b) where Ti and B atoms are red and yellow, respectively. (c) Mean Ti Voronoi intensity, averaged over all atom columns in each (0001) plane T0 to T10 calculated by DetectColumns program [49].

Other facets of the nanoparticles were investigated in a similar manner. Fig. 7a and b shows a pyramidal (01¯11) TiB_2 interfaces, while Fig. 7c and d shows a prismatic (11¯00) TiB_2 interface. Again, no alignment with the Al matrix is present, indicating an incommensurate interface. Interestingly, in all cases a gradation in intensity outside the nanoparticle is present, indicating an interfacial layer <1 nm in thickness with mean atomic number intermediate between Al and Ti. Further investigations were thus carried out using EDX to analyse the composition in more detail. Fig. 8 shows such an analysis of an (0001) TiB_2 interface. This shows that, despite the appearance of a sharp interface in the ADF-STEM image, there is a significant gradient in composition, and a gradually decreasing concentration of Ti outside the TiB_2 particle that extends for roughly 1 nm into the Al matrix. Similarly, EDX data from the pyramidal (01¯11) TiB_2 interface, Fig. 8 f-j, shows a similar Ti–Al gradient as well as a concentration of Cu (~2 at.%) at the matrix/TiB_2 interface. No concentrations of Si or Mg were detected.

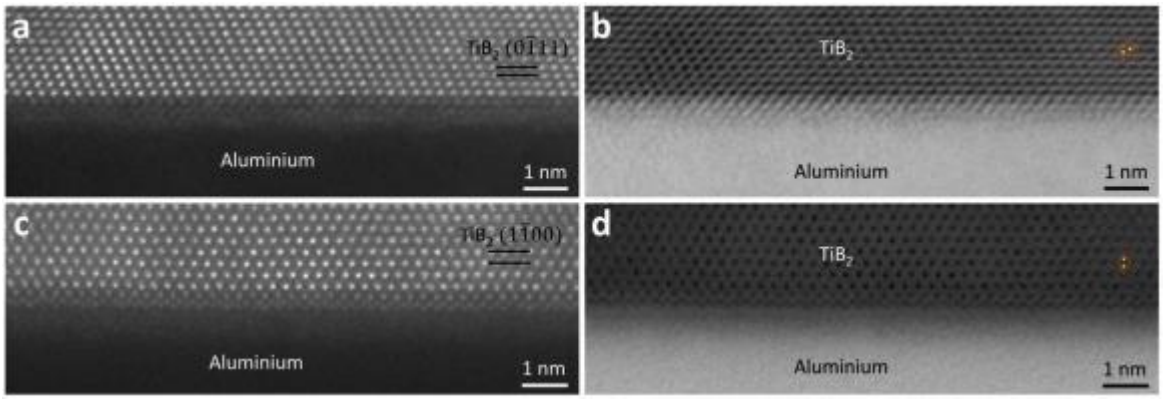

Fig. 7. High resolution STEM images (a, ADF; b, BF) of a pyramidal ($01\bar{1}1$) TiB_2 interface with the incident electron beam along [$11\bar{2}1$]TiB2 and (c, ADF; d, BF) a prismatic ($11\bar{0}0$) TiB_2 interface with the incident electron beam along [0001]TiB2. A model of TiB_2 is superimposed on (b) and (d) with Ti and B atoms are red and yellow, respectively.

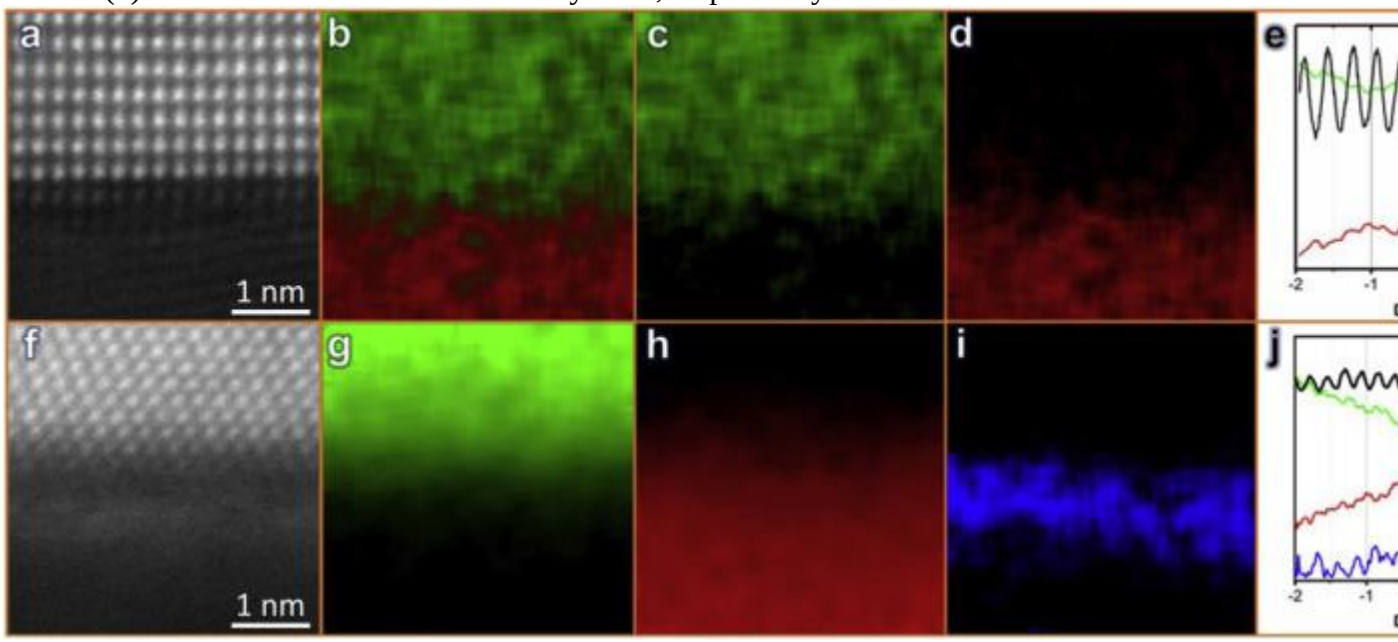

Fig. 8. ADF-STEM images and corresponding chemical maps of Al/TiB_2 interfaces parallel to the TiB_2 (0001) basal plane (a–e) and TiB_2 ($01\bar{1}1$) pyramidal plane (f–j).

3.3. Characterization of β″ precipitates

As is usual in conventional cast Al–Si–Mg alloys, T6 heat treatment [56] induces the formation of needle-shaped β'' precipitates that lie along <100> Al directions. These are too small to be readily detected by X-ray diffraction (Fig. 2). Fig. 9a shows a typical bright-field TEM image with β'' precipitates distributed homogeneously in the Al matrix. With a point of view close to $[100]_{Al}$, β'' precipitates can be seen aligned with the long axis parallel to the

electron beam (embedded) and from the side (lying) precipitates, typically 2–4 nm in diameter and 20–30 nm in length. The corresponding $[001]_{Al}$ SADP is displayed in Fig. 9b, which shows obvious cross-shaped streaks along the <100> Al directions. These observations are in good agreement with previous studies of the monoclinic (*C2/m*) *β″* phase [[57], [58], [59]], with $a = 1.516$ nm, $b = 0.405$ nm, $c = 0.674$ nm, $\beta = 105.3°$ and an orientation relationship:$(010)_{\beta''}//(00\bar{1})_{Al}$, $[001]_{\beta''}//[130]_{Al}$, and $[100]_{\beta''}//[32\bar{0}]_{Al}[01\bar{0}]_{\beta''}//[001]_{Al}$, $(4\bar{0}3)_{\beta''}//(020)_{Al}$, and $(601)_{\beta''}//(200)_{Al}$
Fig. 9c shows a schematic of the two diffraction patterns, $[001]_{Al}$ and $[010]_{\beta''}$. The cross-shaped streaks of the β″ precipitates has been explained by Yang et al. [60] through the ±1-order reciprocal spots, reciprocal lattice rods due to their small dimensions, and double diffraction from 12 orientational variants, producing discontinuous rings, Fig. 9c. Each ring represents a group of β″ crystal planes, i.e. spots on the same ring have the same crystal plane spacing, as shown in Fig. 9c. In this figure brown circles indicate diffraction from variants with an $[010]_{\beta''}$ zone axis while blue circles indicate variants with $[403\bar{}]_{\beta''}$ and $[601]_{\beta''}$ zone axes. An HRTEM image of an embedded β″ precipitate is shown in Fig. 9d, with its corresponding Fourier transform (FT) in Fig. 9e. The red and white circles indicate periodicities of the Al matrix and precipitates, respectively. A simulated $[001]_{Al}$ SADP is shown in Fig. 9f. There is a near coincidence between the $601_{\beta''}$ and 200_{Al} reflections and the $403\bar{}_{\beta''}$ and 020_{Al} reflections. Good agreement with the expected orientation relationship is also obtained for β″ precipitates lying in the specimen plane, as shown in Fig. 9g–i.

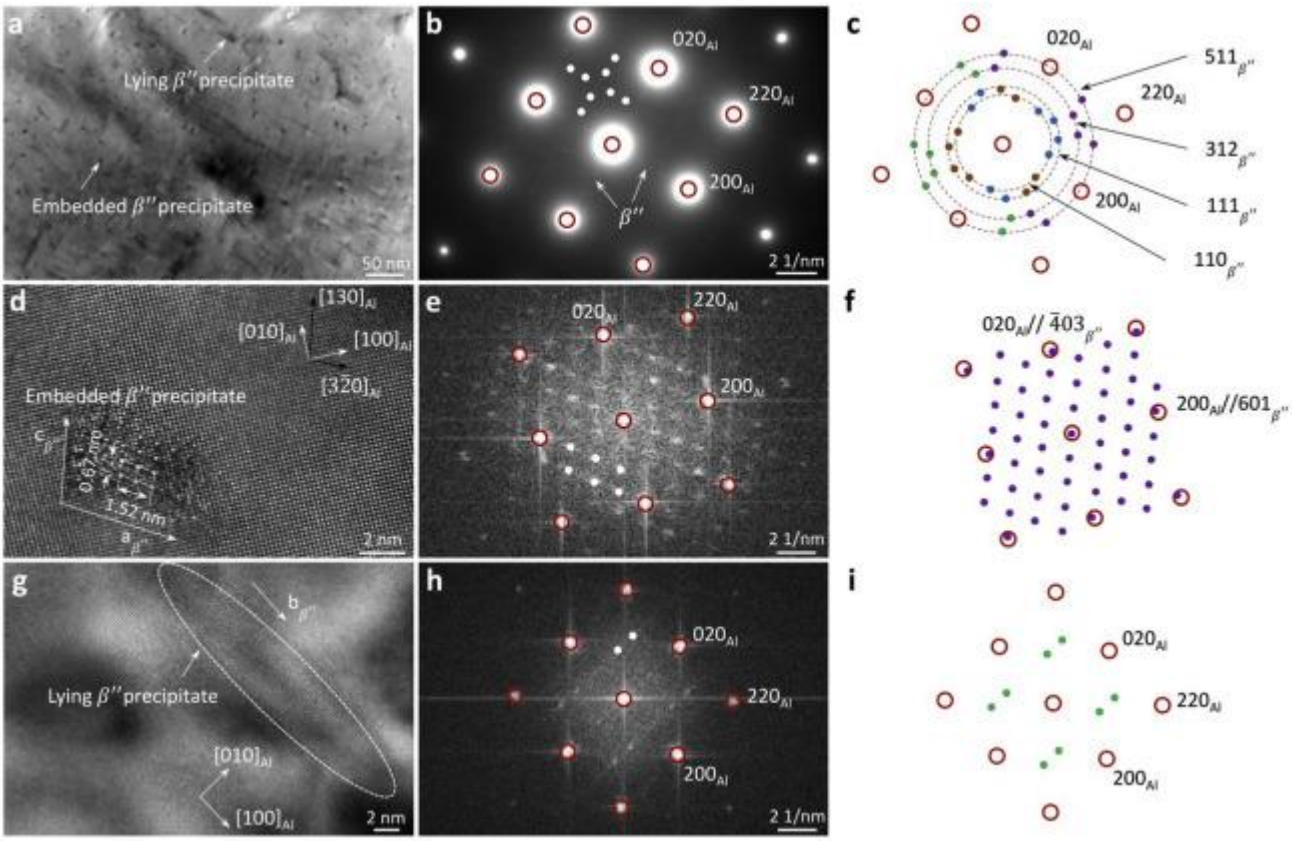

Fig. 9. (a) Bright field TEM image showing lying and embedded β″ precipitates, (b) corresponding SADP; red and white circles indicate reflections from Al matrix and precipitates, respectively, (c) indexed schematic pattern with $[001]_{Al}$ (red circles) and four orientational variants of $[010]_{\beta''}$ (blue, brown, green and purple). (d) HRTEM image of embedded β″ precipitates, (e) corresponding Fourier transform, (f) indexed schematic pattern. (g) HRTEM image of a β″ precipitate lying perpendicular to the beam direction, (h) corresponding Fourier transform, and (i) indexed schematic pattern.

3.4. Mechanical properties

Table 2 shows the mechanical properties of all specimens. As seen, a great enhancement in stiffness, yield strength and ultimate tensile strength of the composite is observed when the reinforcement added to the microstructure. The same behaviour was observed in all other cast composites compared with conventional Al–7Si-0.3 Mg base alloy. The Young's modulus of the nanocomposites, measured by ultrasonic pulse and tensile tests, are shown in Table 2. The stiffness is significantly improved by addition of TiB_2 nanoparticles. The Young's modulus of the Al–10Si-0.3Mg/9 TiB_2 nanocomposite is ~94 GPa, significantly higher than that of the Al–7Si-0.3 Mg reference alloy at ~73 GPa. Table 2 also demonstrates the tensile properties of the Al–7Si-0.3 Mg alloy and Al–Si–Mg/TiB_2 nanocomposites. A large enhancement in the

yield strength and the ultimate tensile strength (UTS) is observed in the alloys reinforced by TiB_2. The yield strength is increased from 230 MPa to over 306 MPa.

Table 2. Density, velocity parameters, Young's modulus and tensile properties of the Al–Si–Mg/TiB_2 nanocomposites.

Material	Density (g/cm^3)	Longitudinal velocity (mm/μs)	Shear velocity (mm/μs)	Poisson's ratio	E^a (GPa)	E^b (GPa)	YS (MPa)	UTS (MPa)	Elongation (%)
Al–7Si-0.3 Mg	2.65	6.31	3.25	0.31	73.9	73.1	230	262	4.3
Al–10Si-0.3 Mg	2.65	6.30	3.24	0.31	73.9	73.1	235	267	4.2
Al–7Si-0.3Mg/8 vol% TiB_2	2.79	6.70	3.47	0.31	88.7	88.4	306	340	2.2
Al–7Si-0.3Mg/9 vol% TiB_2	2.80	6.79	3.54	0.31	92.4	91.8	314	344	2.2
Al–10Si-0.3Mg/9 vol% TiB_2	2.80	6.78	3.58	0.31	94.1	93.5	322	348	2.1

a Dynamic method, ultrasonic pulse technique.

B Static method, tensile test.

4. Discussion

The above results demonstrate the successful production of Al–Si–Mg/TiB_2 nanocomposites with relatively homogeneous distribution of the TiB_2 particles. They also show the characteristics of different interfaces between TiB_2 nanoparticles and aluminium matrix, i.e. interfaces which are parallel to basal, prismatic and pyramidal planes of the TiB_2 nanoparticles. The nanocomposites have superior mechanical properties, with Young's modulus over 90 GPa and YS > 300 MPa. As the mechanical properties of the produced nanocomposites are strongly influenced by the matrix/TiB_2 interfacial characteristics, different aspect of the interfaces will be discussed in this section. Also, mechanisms for improvement of stiffness and strength, and contribution of each mechanism will be compared to experimental results and micromechanics-based theoretical analysis.

We found that most TiB_2 particles in our material had random crystallographic orientation relationships (OR) with the Al matrix. This may be due to their relatively high density and is consistent with the free growth model which predicts that only 0.1–1% of the TiB_2 particles participate in heterogeneous nucleation [61]. For high resolution electron microscopy, the lack of a definite OR makes it difficult to reveal the atomic structure at the interface in both matrix and nanoparticle. Nevertheless, the atomic number sensitivity of ADF-STEM images clearly shows a gradation in atomic number that extends up to 1 nm into the Al matrix from the edge of the TiB_2 nanoparticle, as defined by the edge of the crystal lattice. This appears to be present at all interfaces and is visible in Fig. 5, Fig. 6, Fig. 7, Fig. 8. However, there are differences between the different facets, which will be discussed in turn below.

4.1. Interface parallel to the basal (0001) plane of TiB_2

Atomic resolution ADF-STEM images of this interface show an interface that does not appear atomically abrupt; the TiB_2 lattice fades away over 2 or 3 monolayers, rather than ending at a single (0001) TiB_2 plane. Since the STEM image is a projection, it is not immediately obvious whether this is due to interfacial roughness (i.e. crystal planes that do not extend through the full thickness of the TEM specimen), or a change in composition (i.e. substitution of Ti with Al). The EDX analysis (Fig. 5) shows that the Ti content decreases more gradually than the ADF contrast, and is matched by a similar gradual increase in Al content. The atomic resolution and abruptness of the ADF image shows that this cannot be accounted for by spreading of the beam through the specimen (~70 p.m. in diameter when incident on the uppermost surface) and is therefore a real gradient in Al–Ti composition. Furthermore, the Al signal is some way from zero at the outermost atomic layer of the particle, suggesting that perhaps ~20% of the Ti has been substituted by Al to give $Al_{0.2}Ti_{0.8}B_2$. It has been suggested [27,62,63] that a monolayer of Al_3Ti forms on TiB_2 basal facets, which is clearly not the case here, unlike the data of Fan et al. [27]. This difference may be due to the in-situ formation of TiB_2 nanoparticles in our case, in contrast with the addition of pre-formed TiB_2 in commercial grain refiner (Al–Ti–B) and deliberate Ti excess used by Fan et al. [27]. Furthermore, our complex alloy containing Si, Mg, Cu, Ti, Fe and Mn elements solidifies thermodynamically different compared with that of pure Al alloy investigated by Fan et al. [27]. Here, it seems most likely that the segregation of Ti in the Al matrix to the immediate vicinity of the nanoparticle occurred on cooling [64]. The presence of a Ti gradient external to the nanoparticle is likely to be beneficial for mechanical properties since it will increase Peierls stresses on dislocations while avoiding abrupt changes in elastic moduli that could initiate rupture under stress.

4.2. Interface parallel to the pyramidal $(01\bar{1}1)$ plane of TiB_2

For improvements in mechanical strength, the constitution of all significant TiB_2 facets is of interest, particularly since it has been shown that particle morphologies can be altered significantly by different processing conditions [65,66]. The EDX data (Fig. 8j) shows that gradients in the Al and Ti content over a few nm are also present at this interface. While the $\{011\bar{1}\}$ facets are relatively small on our particles, they show an unexpected layer of Cu (reaching concentrations of ~2 at.%) in the matrix roughly 0.5 nm from the surface of the TiB_2 particle. This indicates that different facets may have quite different chemistry and mechanical properties. The effect of this segregated layer on mechanical properties has yet to be investigated, but one may expect similar hardening benefits from Cu alloying into the Al matrix by reducing dislocation mobility and an elastic modulus intermediate between matrix and nanoparticle.

4.3. Interface parallel to the prismatic $(01\bar{1}0)$ plane of TiB_2

Unfortunately, no EDX data was obtained from the prismatic interface. Nevertheless, the ADF and BF STEM images (Fig. 7c and d) again show a gradation in atomic number outside the nanoparticle, indicating segregation of Ti and possibly Cu to the nanoparticle.

4.4. Stiffness improvement by TiB_2 nanoparticles

Table 2 shows the Young's modulus of the Al–10Si-0.3Mg/9 vol% TiB_2 nanocomposite to be $E \approx 94$ GPa, ~27% higher than that of conventional aluminium alloys ($E \approx 73$ GPa). This is obviously due to the high modulus ($E = 565$ GPa) TiB_2 phase with strongly covalent B–B bonds and ionic-covalent Ti–B bonds [14]. The rule of mixtures (ROM), overestimates the improvement in Young's modulus ($E \approx 120$ GPa), while the inverse ROM underestimates it ($E \approx 80$ GPa). The more sophisticated Halpin-Tsai model [46] takes into account the aspect ratio of the hard nanoparticles,
i.e.$$E = E_m(1+2\xi\eta V_p)/(1-\eta V_p) \quad (8)\ \eta = (E_p/E_m-1)/(E_p/E_m+2\xi)$$where Ep and Em are the Young's modulus of the particles and the matrix, respectively. Vp is the volume fraction of the particles, ξ is the aspect ratio of the particulate reinforcement. Using an aspect ratio of 1.5 for the TiB_2 nanoparticles, equation (7) gives $E = 94.1$ GPa for the Al–10Si-0.3Mg/9 vol. TiB_2 composite, is in good agreement with the experimental value of 93.1 GPa.

4.5. Strength improvement

As seen in Table 2, the nanocomposites have high yield strength (YS > 300 MPa) and ultimate tensile strength (UTS>340 MPa). The strengthening mechanisms can be divided into five categories (Table 2). Localised stresses, produced by the difference in the coefficient of thermal expansion (CTE) of the Al matrix and the TiB_2 nanoparticles, can produce dislocation networks. These hinder the movement of slip dislocations during deformation and increase yield strength [67]. The mismatch in elastic modulus may also produce a transitional dislocation region [68] around the reinforcement phase, giving an increase in yield strength. The Orowan mechanism describes pinning of mobile dislocations by the nanoparticles also has significant effect on Yield strength of the composites. Cast Al–Si–Mg-based alloys and composites, can achieve their maximum strength when metastable and coherent β″ phase is precipitated from the Al matrix [69,70]. As shown in Fig. 9, we observed needle-shaped β″ precipitates in our material. This means that in addition to strengthening by TiB_2, the metastable β″ precipitates also contribute to the strength of our material. β″ precipitates and TiB_2 are most effective in blocking the movement of dislocations in both Al alloy and the nanocomposites.

5. Conclusions

Al–Si–Mg-based nanocomposites reinforced with TiB_2 and produced by an industrial low pressure die casting process display significant improvement in both stiffness and strength. TiB_2 nanoparticles formed hexagonal prisms with chamfered edges and corners, an average diameter ~400 nm and were homogeneously distributed in the Al–Si–Mg matrix. The microstructure was investigated using electron microscopy and the results used to inform theoretical models of stiffness and strength improvement in nanocomposites.

The interfaces between Al and TiB_2 nanoparticles are mainly parallel to dense planes of the titanium diboride, including basal {0001}, prismatic $\{11\bar{0}0\}$ and pyramidal $\{01\bar{1}1\}$ planes. We observed that in-situ TiB_2 particles had random crystallographic orientation relationships with the matrix. Our investigation of the TiB_2 interface with atomic resolution STEM showed that the TiB_2 facets have a transitional layer of ~1 nm thickness with graduations between Ti and Al. In addition, we observed a Cu-rich layer of with a thickness of ~0.5 nm at the pyramidal facets of TiB_2 particles. Although the in-situ TiB_2 particles in our nanocomposites do not have coherent interfaces with the matrix, the above mentioned composition gradients at their facets are likely to enhance both mechanical bonding and present obstacles for dislocation movement close to the matrix/nanoparticle interface, thus improving the mechanical properties of the nanocomposites.

There are very few aluminium alloys with both outstanding Young's modulus and yield strength [18,[71], [72], [73], [74]]. Furthermore, the ductility of such Al-based alloys usually is less than 0.5% when the Young's modulus is more than 85 GPa. However, the materials developed in the present study can provide reasonable ductility of 2.1% when the Young's modulus and yield strength reaches 94 GPa and 320 MPa, respectively. This satisfies industrial requirements for stiffness-based components. While β″ precipitates in a commercial cast Al alloys can improve the yield strength, up to 240 MPa, the TiB_2 nanoparticles used in these alloys provide a promising pathway to further improvement of yield strength, 35%, and stiffness, 27%.

Acknowledgment

Financial support from Jaguar Land Rover (JLR) [grant number R33232] is gratefully acknowledged.

References

[1] H. Zhang, H. Springer, R. Aparicio-Fernández, D. RaabeImproving the mechanical properties of Fe–TiB 2 high modulus steels through controlled solidification processes Acta Mater., 118 (2016), pp. 187-195
[2] H. Springer, R.A. Fernandez, M.J. Duarte, A. Kostka, D. RaabeMicrostructure refinement for high modulus in-situ metal matrix composite steels via controlled solidification of the system Fe–TiB 2 Acta Mater., 96 (2015), pp. 47-56
[3] H. Springer, C. Baron, A. Szczepaniak, V. Uhlenwinkel, D. RaabeStiff, light, strong and ductile: nano-structured high modulus steel Sci. Rep., 7 (2017)
[4] I. FridlyanderHigh-modulus aluminum alloys with beryllium and magnesium Met. Sci. Heat Treat., 45 (9) (2003), pp. 348-350
[5] B. Noble, S. Harris, K. DinsdaleThe elastic modulus of aluminium-lithium alloys J. Mater. Sci., 17 (2) (1982), pp. 461-468
[6] F. Lasagni, H.P. DegischerEnhanced Young's modulus of Al-Si alloys and reinforced matrices by Co-continuous structures. J. Compos. Mater., 44 (6) (2010), pp. 739-755
[7] H.A. Hafez, M.M. FaragEffect of structure on the Young's modulus of Al-Cu-Ni alloys J. Mater. Sci., 16 (5) (1981), pp. 1223-1232
[8] D.G. Eskin, L. ToropovaTensile and elastic properties of deformed heterogeneous aluminum alloys at room and elevated temperatures Mater. Sci. Eng., A, 183 (1–2) (1994), pp. L1-L4
[9] K.-i. Masuda-Jindo, K. TerakuraElectronic theory for solid-solution hardening and softening of dilute Al-based alloys: elastic-moduli enhancement of Al-Li alloys Phys. Rev. B, 39 (11) (1989), p. 7509
[10]

A. Villuendas, J. Jorba, A. RocaThe role of precipitates in the behavior of Young's modulus in aluminum alloys
Metall. Mater. Trans. A, 45 (9) (2014), pp. 3857-3865

[11]
T. Nakata, C. Xu, R. Ajima, K. Shimizu, S. Hanaki, T. Sasaki, L. Ma, K. Hono, S. Ka madoStrong and ductile age-hardening Mg-Al-Ca-Mn alloy that can be extruded as fast as aluminum alloys
Acta Mater., 130 (2017), pp. 261-270

[12]
A. Szczepaniak, H. Springer, R. Aparicio-
Fernández, C. Baron, D. RaabeStrengthening Fe–TiB 2 based high modulus steels by precipitations
Mater. Des., 124 (2017), pp. 183-193

[13]
C. Baron, H. Springer, D. RaabeEffects of Mn additions on microstructure and properties of Fe–TiB 2 based high modulus steels
Mater. Des., 111 (2016), pp. 185-191

[14]
S. Lartigue-
Korinek, M. Walls, N. Haneche, L. Cha, L. Mazerolles, F. BonnetInterfaces and defects in a successfully hot-rolled steel-based composite Fe–TiB 2
Acta Mater., 98 (2015), pp. 297-305

[15]
Z. Hadjem-Hamouche, J.P. Chevalier, Y. Cui, F. BonnetDeformation behavior and damage evaluation in a new titanium diboride (TiB2) steel-based composite
Steel Res. Int., 83 (6) (2012), pp. 538-545

[16]
S. Kumar, M. Chakraborty, V. Subramanya Sarma, B.S. MurtyTensile and wear behaviour of in situ Al–7Si/TiB2 particulate composites
Wear, 265 (1) (2008), pp. 134-142

[17]
G. Han, W. Zhang, G. Zhang, Z. Feng, Y. WangHigh-temperature mechanical properties and fracture mechanisms of Al–Si piston alloy reinforced with in situ TiB2 particles
Mater. Sci. Eng., A, 633 (2015), pp. 161-168

[18]
D. LloydParticle reinforced aluminium and magnesium matrix composites
Int. Mater. Rev., 39 (1) (1994), pp. 1-23

[19]
W. Zhou, T. Yamaguchi, K. Kikuchi, N. Nomura, A. KawasakiEffectively enhanced load transfer by interfacial reactions in multi-walled carbon nanotube reinforced Al matrix composites

Acta Mater., 125 (2017), pp. 369-376

[20]
P.K. RohatgiMetal matrix composites
Def. Sci. J., 43 (4) (1993), p. 323

[21]
R.G. MunroMaterial properties of titanium diboride
J. Res. Natl. Inst. Stand. Technol., 105 (5) (2000), p. 709

[22]
K.U. KainerMetal Matrix Composites: Custom-Made Materials for Automotive and Aerospace Engineering
John Wiley & Sons (2006)

[23]
G.P. Jones, J. PearsonFactors affecting the grain-refinement of aluminum using titanium and boron additives
Metall. Trans. B, 7 (2) (1976), pp. 223-234

[24]
A. CibulaThe mechanism of grain refinement of sand castings in aluminium alloys
J. Inst. Met., 76 (4) (1949), p. 321

[25]
P. Davies, J. Kellie, D. Parton, London and Scandinavian Co, Limited, Patent WO 93 (1993) 05189.

[26]
N.L. Yue, L. Lu, M.O. LaiApplication of thermodynamic calculation in the in-situ process of Al/TiB2
Compos. Struct., 47 (1) (1999), pp. 691-694

[27]
Z. Fan, Y. Wang, Y. Zhang, T. Qin, X. Zhou, G. Thompson, T. Pennycook, T. Hashi motoGrain refining mechanism in the Al/Al–Ti–B system
Acta Mater., 84 (2015), pp. 292-304

[28]
K. Tee, L. Lu, M. LaiIn situ stir cast Al–TiB2 composite: processing and mechanical properties
Mater. Sci. Technol., 17 (2) (2001), pp. 201-206

[29]
A. Mandal, M. Chakraborty, B. MurtyAgeing behaviour of A356 alloy reinforced with in-situ formed TiB 2 particles
Mater. Sci. Eng., A, 489 (1) (2008), pp. 220-226

[30]
S. Kumar, M. Chakraborty, V.S. Sarma, B. MurtyTensile and wear behaviour of in situ Al–7Si/TiB 2 particulate composites
Wear, 265 (1) (2008), pp. 134-142

[31]

S.H. Nandam, S. Sankaran, B. MurtyPrecipitation kinetics in Al-Si-Mg/TiB2 in-situ composites
Trans. Indian Inst. Met., 64 (1–2) (2011), pp. 123-126

[32]
G.V. Kumar, B. Murty, M. ChakrabortyDevelopment of Al–Ti–C grain refiners and study of their grain refining efficiency on Al and Al–7Si alloy
J. Alloy. Comp., 396 (1) (2005), pp. 143-150

[33]
B. Yang, Y. Wang, B. ZhouThe mechanism of formation of TiB2 particulates prepared by in situ reaction in molten aluminum
Metall. Mater. Trans. B, 29 (3) (1998), pp. 635-640

[34]
F. Chen, Z. Chen, F. Mao, T. Wang, Z. CaoTiB 2 reinforced aluminum based in situ composites fabricated by stir casting
Mater. Sci. Eng., A, 625 (2015), pp. 357-368

[35]
S. Kumar, V.S. Sarma, B. MurtyEffect of temperature on the wear behavior of Al-7Si-TiB2 in-situ composites
Metall. Mater. Trans. A, 40 (1) (2009), pp. 223-231

[36]
G. Han, W. Zhang, G. Zhang, Z. Feng, Y. WangHigh-temperature mechanical properties and fracture mechanisms of Al–Si piston alloy reinforced with in situ TiB 2 particles
Mater. Sci. Eng., A, 633 (2015), pp. 161-168

[37]
Y. Zhang, N. Ma, H. Wang, Y. Le, X. LiDamping capacity of in situ TiB 2 particulates reinforced aluminium composites with Ti addition
Mater. Des., 28 (2) (2007), pp. 628-632

[38]
H.M. Rajan, S. Ramabalan, I. Dinaharan, S. VijayEffect of TiB 2 content and temperature on sliding wear behavior of AA7075/TiB 2 in situ aluminum cast composites
Arch. Civ. Mech. Eng., 14 (1) (2014), pp. 72-79

[39]
S. Kumar, V.S. Sarma, B. MurtyInfluence of in situ formed TiB 2 particles on the abrasive wear behaviour of Al–4Cu alloy
Mater. Sci. Eng., A, 465 (1) (2007), pp. 160-164

[40]
S. Kumar, V.S. Sarma, B. MurtyA statistical analysis on erosion wear behaviour of A356 alloy reinforced with in situ formed TiB 2 particles
Mater. Sci. Eng., A, 476 (1) (2008), pp. 333-340

[41]

S. Kumar, V.S. Sarma, B. MurtyFunctionally graded Al alloy matrix in-situ composites
Metall. Mater. Trans. A, 41 (1) (2010), pp. 242-254
[42]
S. Kumar, V.S. Sarma, B. MurtyThe influence of room temperature and cryogenic temperature rolling on the aging and wear behaviour of Al–4Cu–5TiB 2 in situ composites
J. Alloy. Comp., 479 (1) (2009), pp. 268-273
[43]
A. Mandal, B. Murty, M. ChakrabortyWear behaviour of near eutectic Al–Si alloy reinforced with in-situ TiB 2 particles
Mater. Sci. Eng., A, 506 (1) (2009), pp. 27-33
[44]
S. Kumar, V.S. Sarma, B. MurtyHigh temperature wear behavior of Al–4Cu–TiB 2 in situ composites
Wear, 268 (11) (2010), pp. 1266-1274
[45]
S. Amirkhanlou, S. Ji, Y. Zhang, D. Watson, Z. FanHigh modulus Al Si Mg Cu/Mg 2 Si TiB 2 hybrid nanocomposite: microstructural characteristics and micromechanics-based analysis
J. Alloy. Comp., 694 (2017), pp. 313-324
[46]
M. Wang, D. Chen, Z. Chen, Y. Wu, F. Wang, N. Ma, H. WangMechanical properties of in-situ TiB 2/A356 composites
Mater. Sci. Eng., A, 590 (2014), pp. 246-254
[47]
ASTM B108/B108M-15Standard Specification for Aluminum-Alloy Permanent Mold Castings ASTM International, West Conshohocken, PA (2015)
[48]
M. Merlin, G. Timelli, F. Bonollo, G.L. GaragnaniImpact behaviour of A356 alloy for low-pressure die casting automotive wheels
J. Mater. Process. Technol., 209 (2) (2009), pp. 1060-1073
[49]
A. Mostaed, G. Balakrishnan, M.R. Lees, Y. Yasui, L.-J. Chang, R. BeanlandAtomic structure study of the pyrochlore $Yb_2Ti_2O_{-7}$ and its relationship with low-temperature magnetic order Phys. Rev. B, 95 (9) (2017), p. 094431
[50]
ASTM E1875-13Standard Test Method for Dynamic Young's Modulus, Shear Modulus, and Poisson's Ratio by Sonic Resonance
ASTM International, West Conshohocken, PA (2013)
[51]

F. Bonnet, V. Daeschler, G. PetitgandHigh modulus steels: new requirement of automotive market. How to take up challenge?
Can. Metall. Q., 53 (3) (2014), pp. 243-252